This article has been accepted for publication in a future issue of this journal, but has not been fully edited. Content may change prior to final publication. Citation information: DOI 10.1109/TAP.2014.2364052, IEEE Transactions on Antennas and Propagation

A Wideband CPW-fed Planar Dielectric Tapered Antenna with Parasitic Elements for 60 GHz Integrated Application

Saman Jafarlou, *Member, IEEE,* Maher Bakri-Kassem, Mohammad Fakharzadeh, *Senior Member, IEEE*, Zahra Sotoodeh and Safieddin Safavi-Naeini.

***Abstract*—This paper presents a high-efficiency wideband planar dielectric tapered antenna designed for 60 GHz integrated applications fabricated through a novel process compatible with silicon technology. The antenna is composed of five parts: a CPW line, a balun, a tapered slot line, a dielectric tapered antenna and parasitic elements. Single antenna has a simulated impedance bandwidth from 52.4 GHz to 66.4 GHz, and a peak gain between 8.5 dBi to 10.25 dBi over the bandwidth. Furthermore, a two element array of this antenna is designed using a CPW power divider with a simulated 12 dBi gain and 9 GHz bandwidth. Single element antenna and two element array prototypes are fabricated on high-resistive bonded silicon wafers through a novel eleven-step fabrication process designed for double-sided etching. The measured results of single antenna show over 15 GHz bandwidth and 9.6 dBi gain. For the two element array measured the bandwidth and gain are 10 GHz and 10.8 dBi, respectively. The antenna performance is suitable for integrated mm-wave applications requiring wide bandwidth, particularly mm-wave imaging.**

***Index Terms*—60 GHz, array antenna, dielectric rod antenna, integrated application, silicon fabrication process, tapered slot antenna.**

I. Introduction

OVER the last decade, millimetre-wave (mm-wave) front end circuits have attracted enormous attention in high speed, short range wireless applications. Significant efforts have been made on standardization and development of active and passive devices at the unlicensed 60 GHz spectrum ranging from 57 GHz to 66 GHz [1]. An efficient, broadband and directional antenna is a key element of such systems. Many metallic antennas have been presented with high radiation gain [2, 3] at mm-wave frequency range; however, the relatively narrow bandwidth of these antennas limits the range of applications. In [4], a 16 element array of patch antennas with embedded cavities has been presented with 18.2 dBi gain and less than 10 % impedance bandwidth. Despite high directivity of such structures, the efficiency is fairly low due to the noticeable conductor loss and complex feed network. For instance, in [5] a configuration of patch antennas has been proposed to achieve 15 dBi radiation gain for a 16 element array, while the efficiency is 43% and the bandwidth is only 2 GHz. Compared to broadside antennas, endfire antennas are more attractive for wide-band beam switching applications and low-profile systems. [6, 7]. For example, a microstrip-fed Yagi-Uda antenna on low-permittivity RT/Duroid substrate is reported with 10 GHz bandwidth and 9.5 dBi gain in [7].

On the other hand, dielectric rod antenna (DRA) is a promising alternative for the applications requiring wide impedance bandwidth, high radiation efficiency, and stable radiation pattern over the frequency [8, 9]. Nevertheless, the challenge is to design a proper feed for DRA that maintains a smooth transition of power to the antenna [10]. A wideband feed technique is to taper one end of the DRA and insert it into a metallic waveguide or horn antenna [11]; however, it leads to a bulky and costly solution. In [12] the rod antenna is excited by a tapered slot with a wide bandwidth from 3.1 to 10.6 GHz. Recently, substrate-integrated waveguide (SIW) structures have been investigated to feed DRAs [13]. Furthermore, in [14] a substrate integrated non-radiative dielectric (SNIR) on Alumina is used to feed a 7 mm long rod antenna with 9.5 dBi gain at 94 GHz providing 10 GHz bandwidth. Integrated horn has been used to feed tapered slot antennas [15] connected in a non-planar form resulting in 16 dBi gain in the frequency band of 57-66 GHz.

These methods are barely suitable for integrated planar configurations, such as IC flip chipping or MEMS assembly, due to the lack of ground-signal-ground (GSG) connecting pads. Therefore, CPW feed structures are of special interest for high frequency active components integration. Accordingly, a transition from CPW to a substrate integrated image guide (SIIG) feeding a dielectric rod antenna on a Alumina substrate is proposed in [16]. For this structure 11.5 dBi gain, 80 % efficiency and 10 GHz impedance bandwidth is reported. Nevertheless, using Alumina substrate in MEMS fabrication processes is not preferred because of difficulty in cutting and shaping. Therefore, in this work we use high-resistive silicon substrate to take the advantage of monolithic fabrication process with other devices.

The proposed antenna is a planar implementation of dielectric tapered rod antenna on silicon fed by a CPW line. Using a high permittivity dielectric such as silicon reduces the rod length for a certain gain. To simplify the fabrication process, only in-plane tapering is applied that leads to a relatively narrower beam in that plane [10]. Another advantage

S. Jafarlou and M. Fakharzadeh are with Peraso Tech Inc., Toronto, Ontario M5J 2L7, Canada.
E-mail: sjafarlo@uwaterloo.ca
S. Safavi-Naeini and Z. Sotoodeh are with the department of Electrical and Computer Engineering of the University of Waterloo, Waterloo, Ontario N2L 3G1, Canada.
M. Bakri-Kassem is with American University of Sharjah.
Manuscript received February 19, 2013.

This article has been accepted for publication in a future issue of this journal, but has not been fully edited. Content may change prior to final publication. Citation information: DOI 10.1109/TAP.2014.2364052, IEEE Transactions on Antennas and Propagation

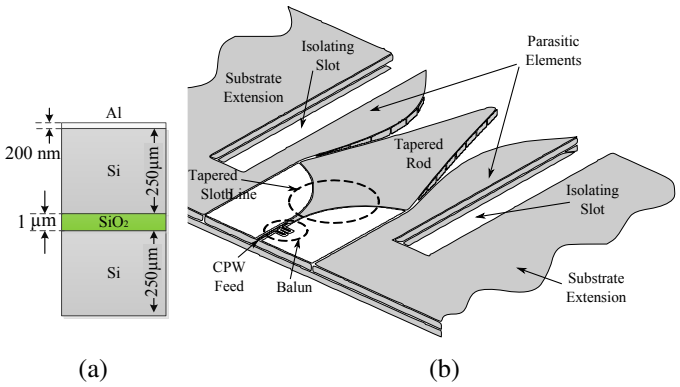

Fig. 1. (a) Cross section of the substrate consisted of a silicon dioxide layer sandwiched between two silicon wafers and an aluminium layer on top, (b) side view of the antenna and its different parts.

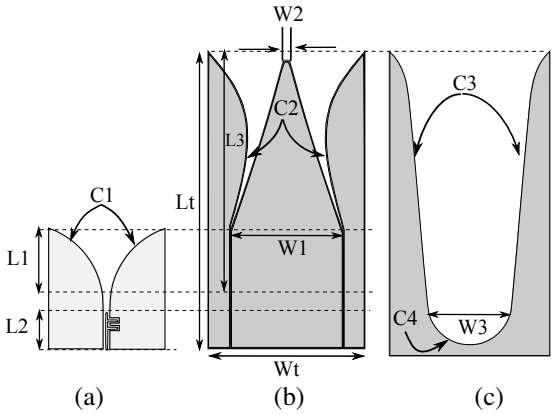

Fig. 2. Patterns etched on (a) aluminium layer, (b) top silicon layer and (c) bottom silicon layer (SiO_2 layer is a uniform plane)

of the proposed antenna structure is to enhance the mechanical robustness and facilitate the packaging process, whereas packaging of the conventional fragile dielectric rod antennas is challenging.

The organization of the paper is as follows. In Section II, a single CPW fed tapered rod antenna, its building blocks, and a two-element array of this antenna are discussed. In Section III, the simulation results of the proposed antennas are presented. Section IV describes the developed fabrication process of the antennas. In Section V, first the measurement setup is described, and the measured results are reported and compared with simulation. Finally, Section VI concludes the paper.

II. Antenna Configuration

Dielectric tapered rod antennas are very well known type of travelling wave antennas that can provide wide operation bandwidth along with high efficiency [17]. However, the planar implementation of dielectric tapered antenna for integrated applications has certain challenges such as mechanical robustness during fabrication processes and packaging. In order to address these issues, in this paper, the antenna is built in such a way that the tip of the rod is not blocked by any silicon material from the used silicon substrate, as shown in Fig. 1(b). This also requires less packaging effort compared to other designs in which a thin and fragile rod extrude out of the substrate [14]. Fig. 1(b) shows the presented antenna consisting of a feed section, tapered rod and parasitic elements. The antenna can be used in presence of the substrate extension providing that two isolating slots are etched next to the parasitic elements to suppress the coupling of energy to the substrate surface modes.

The proposed antenna is built from two 250 μm high-resistive silicon wafers bonded with a 1 μm thick oxide layer as illustrated in Fig. 1(a). A 200 nm thick aluminum layer is also deposited and patterned on top of the substrate. This configuration provides the possibility of etching both, the top and bottom silicon layers with different patterns, as described in Section VI, to achieve desired performance. The relative permittivity of the silicon and silicon dioxide are 11.9 and 4, respectively. Since the length of the tapered antennas mainly determines the gain and side lobe level of the antenna [18], high permittivity of silicon allows for shorter realization of the tapered rod antenna.

TABLE I
Dimension of Antenna

Parameter	Value (mm)
$L1$	1.67
$L2$	4.9
$L3$	8.0
Lt	9.3
Wt	4.9
$W1$	3.5
$W2$	0.2
$W3$	2.5

Tapered rod is the main part of the antenna which is etched out of the top silicon layer with length of $L3$ and initial width of $W1$ tapering linearly to $W2$ at the tip, as shown in Fig. 2. The parasitic dielectric elements are implemented in top silicon layer to increase the antenna radiation gain by enlarging the effective antenna aperture [19]. There is a 20 μm groove between the parasitic elements and rod which is widened along a curve, C2. Therefore, the total dimension of the antenna is $Lt \times Wt$. To keep these elements attached, a supporting structure is implemented in bottom silicon layer, as illustrated in Fig. 2(c). This layer is etched at the bottom of tapered rod, through C3 and C4 curves, to minimize the disturbance effect of this structure on the electromagnetic field.

Fig. 2(a) shows the antenna feed etched on the aluminum layer consists of three parts, namely CPW line, an F-shape balun and a tapered slot line. The antenna is fed by a 50 Ω CPW line on the aforementioned substrate with W_{line} = 80 μm and W_{gap} = 40 μm and is connected to the F-shape balun which is a transition from CPW to a W_{slot}= 160 μm slot line. This slot line is widened to $W1$ through a circular arc, C1, acting as a tapered slot antenna, as shown in Fig. 2(a) to transfer the energy into dielectric [12]. Thus, the E-plane and H-plane of the antenna are parallel and normal to the substrate, respectively.

Fig. 3 illustrates a two-element array of the antennas con-

This article has been accepted for publication in a future issue of this journal, but has not been fully edited. Content may change prior to final publication. Citation information: DOI 10.1109/TAP.2014.2364052, IEEE Transactions on Antennas and Propagation

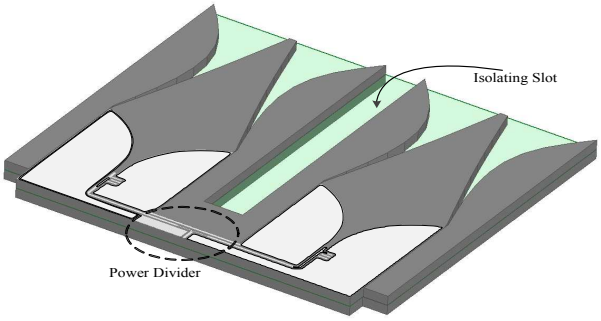

Fig. 3. Two-element array antenna with 6 mm spacing connected by the CPW power divider.

nected by a power combiner/splitter. The distance between the array elements is 6 mm as shown in Fig. 3, and an isolating slot is implemented between antennas to decrease the inter-coupling of antennas.

III. Simulation Results

The simulation of the proposed tapered dielectric antennas is conducted by the finite element method offered in Ansys HFSS.

A. Balun design

The F-shape transition part changes the field distribution of CPW to slot line by introducing 180° phase delay to one side of the CPW in F-shape meandering [20]. From a simple calculation, the propagation wavelength of the CPW line obtained is around 2 mm, so the total length of the meandering must be 1 mm. To get more compact size and field confinement this length is added in two stages creating an F-shape with a length of 0.25 mm. The optimized parameters obtained from full-wave simulation are reported in Fig. 4. The simulated results of the insertion loss of the balun show very wideband operation, from 52 GHz to 70 GHz, with insertion loss of 0.6 dB as presented in Fig. 4.

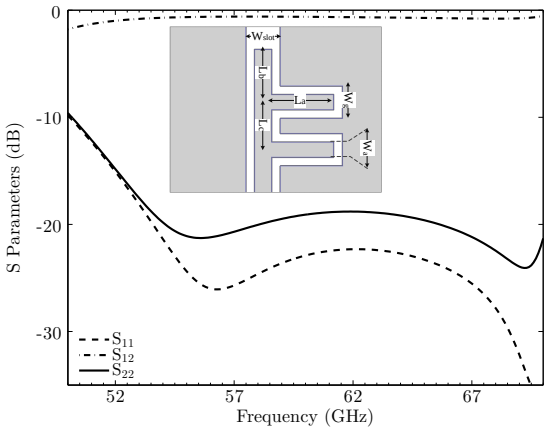

Fig. 4. Simulated scattering parameters of the F-shape balun, W_{slot} = 160 μm, W_g = 150 μm, W_a = 70 μm, L_a = 290 μm and L_b = L_c = 220 μm.

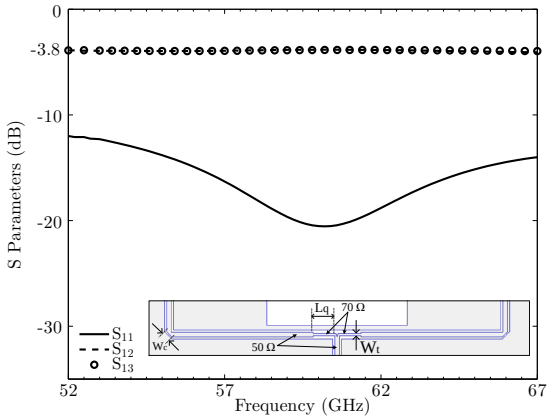

Fig. 5. Top view of the 1-to-2 power divider and corresponding impedances of the lines and the simulated results, Lq = 425 μm, Wt = 40 μm and Wc = 190 μm.

B. Power divider

The two-element array of the proposed antenna is designed to be excited by a 1-to-2 power divider. Fig. 5 shows the power divider and impedances corresponding to the CPW lines at the junctions. Two 70 Ω quarter-wavelength transformers are added to convert the 50 Ω impedance of each line to 100 Ω. These two 100 Ω input impedance are in parallel and matched with 50 Ω at the T-junction. CPW lines are bended by the chamfering dimensions presented in [21]. All the dimensions are optimized for minimum insertion loss through full wave simulations in HFSS. The results presented in Fig. 5 show a bandwidth of more than 15 GHz covering all desired spectrum and an insertion loss of less than 0.8 dB. Based on simulation, the insertion loss per unit length for CPW is 0.12 dB/mm resulting in 0.35 dB loss at T-junction.

C. Optimized antenna design

In this Section a comparison between different possible designs is made and a guideline for designing the proposed antenna is presented. The main part of the antenna is the tapered rod part (shape (a) in Fig. 6). In this design, we added two parasitic elements to the main tapered rod in E-plane to increase the directivity of the antenna through increasing the effective aperture size (shape (b) in Fig. 6). As a result the radiation gain increased by 2.5 dB, but it costs 40% increase in silicon real state. On the other hand, the simulations show that the radiation pattern of the antenna is not affected in presence of extension of substrate with two isolating slots on both sides. These slots, which are also applied in the array configuration, have 1.1 mm width and 7 mm length to reduce the coupling.

Table I shows the optimized parameters of the antenna designed, illustrated in Fig. 2, for 60 GHz to achieve the maximum bandwidth. The other optimization goal was to maintain the peak gain above 10 dBi. The balun design is presented in Section III-A. A tapered slot antennas with a circular curve, C1, of 1.67 mm radius is excited by the balun. HFSS simulations show that the curved tapering of the rod does not have significant impact on the impedance bandwidth of the antenna. Furthermore, side parasitic elements

This article has been accepted for publication in a future issue of this journal, but has not been fully edited. Content may change prior to final publication. Citation information: DOI 10.1109/TAP.2014.2364052, IEEE Transactions on Antennas and Propagation

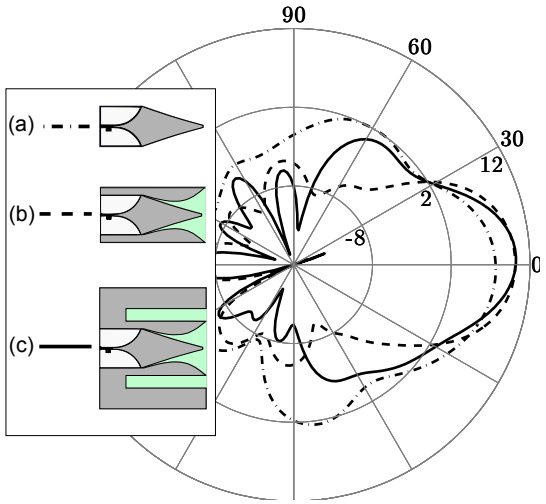

Fig. 6. E-plane radiation pattern of three configuration: single rod without parasitic elements, single rod with parasitic elements, and single rod with parasitic elements and substrate extension.

and bottom support consist of various curves, C2-C4, to provide a smooth transition of the wave from tapered slot to dielectric, and then to free space. These curves are optimized to maximize the bandwidth of the antenna.

The length of tapered rod antenna, $L3$, is a major parameter of the dielectric rod antennas, which is determined based on a trade-off between gain and mechanical strength of the structure. Fig. 7 presents the peak gain of antenna with respect to $L3$ excited by a slot line. For each length, the C2 and C3 curves are modified to obtain the desired bandwidth from 52 GHz to 67 GHz. Parametric studies show that the desired bandwidth is hardly achieved for $L < 7$ mm. On the other hand, minimum 10 dBi gain is not obtained for $L3 < 8$ mm. To have the shortest size which leads to maximum mechanical strength, $L3 = 8$ mm is chosen as the optimal rod length.

D. Antenna radiation characteristics

Fig. 8 shows the distribution of electric field on the silicon dioxide layer. It reveals how energy transfers from slot into

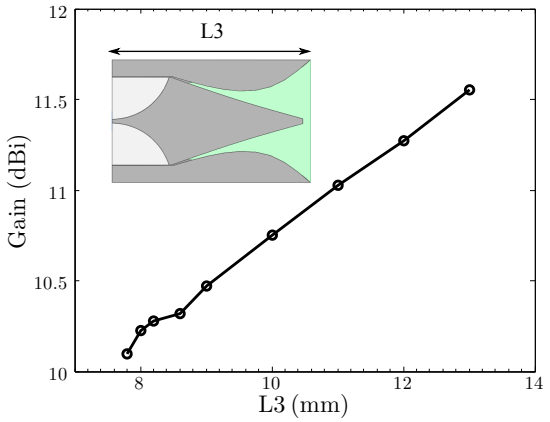

Fig. 7. Simulated peak gain of antenna excluding balun with respect to the length.

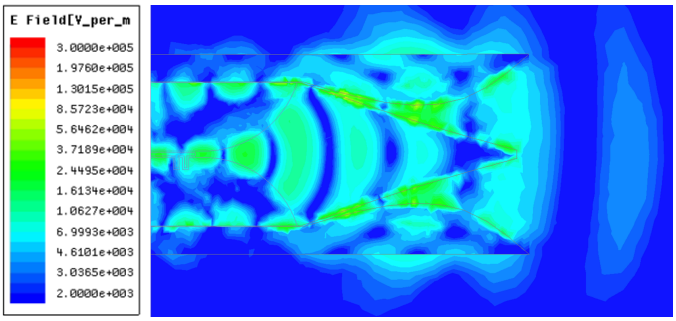

Fig. 8. Electric field distribution on the middle SiO_2 layer.

the dielectric forming a circular wave front. As the wave propagates along the rod, the energy couples to the gap between the side dielectric parts and the rod. Eventually the wave creates a relatively planar wavefront at the tip providing an endfire radiation along the substrate plane.

The bandwidth of antenna defined as $S_{11} < -10$dB is 14 GHz from 52.4 GHz to 66.4 GHz as shown in Fig. 9(a). Furthermore, the pattern of the antenna E- and H-plane are presented in Fig. 9(b) and the gain is 10.25 dB at 60 GHz. It can be seen that H-plane pattern is slightly tilted which is due to asymmetric configuration of CPW-to-slot transition. The 3-dB beamwidth of the antenna in E- and H-plane are 38 deg and 68 deg, respectively. As shown in Fig. 9(b,c,d), the pattern of antenna at 56 GHz, 60 GHz and 64 GHz does not change significantly except the peak gain varying between 9.2 dBi to 10.5 dBi over the whole range. Fig. 9(c) also shows the efficiency and maximum gain versus frequency. Simulation results in Fig. 9(b) show the antenna radiation efficiency is more than 92.5%, also the gain of antenna is above 8.5 dB over the frequency range.

The simulation results of the two element array of antenna, described in previous section, are presented in Fig. 10. It can be seen that the bandwidth of the antenna array is from 52 GHz to 61 GHz. The peak gain of the antenna is 12 dB, which is 1.25 dB less than the expected value considering single element antenna. The element spacing is 6 mm which is larger than a half wavelength. This leads to the grating lobes at +/- 36 deg with -11 dB level. As shown in Fig. 10(d), the efficiency of the antenna is dropped by almost 13% compared to the single element antenna due to the loss of the power divider.

IV. Fabrication Process

High resistive silicon wafers of 250 μm thick and 5000 Ωm are used to fabricate the proposed antennas, the fabrication steps of the proposed antennas are illustrated in Fig. 11. Two bonded wafers of 250 μm thick each and an oxide box in between are used to fabricate the antenna. The first wafer goes through an oxidation step of 1 μm in a furnace at 1000 °C then a temporary bonding is created using a bonding machine before bonded wafers go to the furnace again for permanent bonding at 1000 °C. As a result, both sides, the front and the back sides, have an oxide layer of 1.2 μm and 1μm,

This article has been accepted for publication in a future issue of this journal, but has not been fully edited. Content may change prior to final publication. Citation information: DOI 10.1109/TAP.2014.2364052, IEEE Transactions on Antennas and Propagation

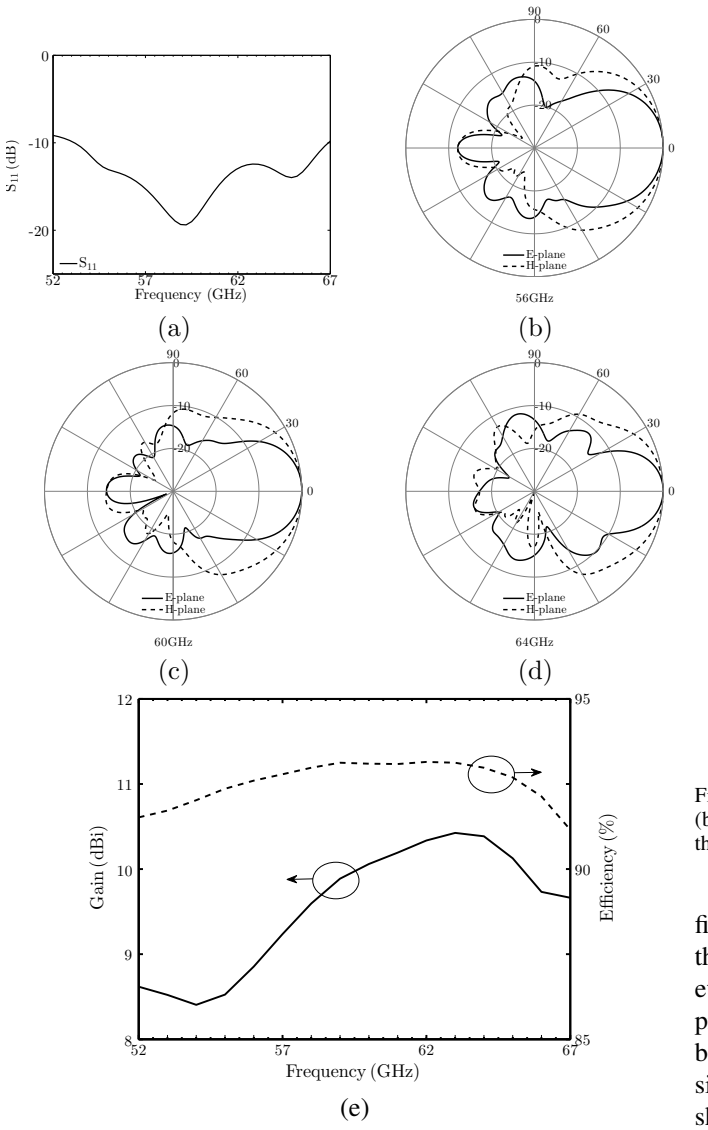

Fig. 9. Simulation results for single antenna design (a) reflection coefficient, radiation pattern of at (b) 56 GHz, (c) 60 GHz and (d) 64 GHz, (e) radiation efficiency and peak gain versus the frequency.

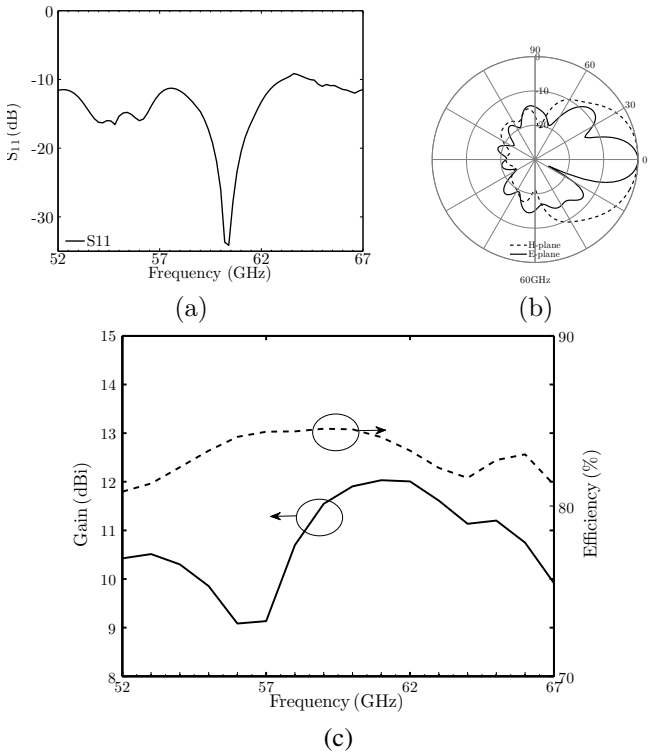

Fig. 10. Simulation results for two element array (a) reflection coefficient, (b) radiation pattern at 60 GHz, (c) peak gain and radiation efficiency versus the frequency.

respectively. Cr/Al layers are then sputtered on the front side with a thickness of 45 nm/1.4 μm as shown in Fig. 11(c) while a second Chrome layer of 60 nm is sputtered on the back side of the bonded wafers. The Chrome layer for the front side will be acting as an adhesion layer for the aluminium layer. The aluminium layer is the metallization layer for the antenna. Photo-resist is spun coating both sides of the bonded wafers. The photo-resist on the front side is used to pattern the antennas metallization layer that is made of the Cr/Al while the photo-resist on the back side is used at this stage to protect the chrome layer on the back side from being etched away during patterning the front side as shown in Fig. 11(e). The photo-resist is then stripped away from both sides and new photo-resist layers are spun coating both sides again to pattern the silicon layers of both sides as shown in Fig. 11(h). DRIE etching is implemented on the front side to etch away the 250 μm thick silicon. The oxide box that was achieved during the first oxidation is used as the etch stop during the silicon etch of the front side. The back side silicon of 250 μm is then DRIE etched as shown in Fig. 11(j). The last step in the fabrication process is to etch away the Cr layer on the back side of the bonded wafers as shown in in Fig. 11(k). The prototypes of single and array antennas fabricated through this process are shown in Fig. 12

V. Measurement Results of the Prototype Antennas

A. Antenna Measurement Setup

The setup used to measure the maximum gain, radiation pattern and the reflection coefficient of the antenna is shown in Fig. 13. The AUT is placed on YZ plane and excited by a 175 μm pitch GSG probe mounted on the air suspended table placed inside the anechoic chamber. Since the AUT has end-fire pattern along Z-axis, some measures must be taken to decrease the disturbance on the radiation such as covering table with absorber and placing the AUT on a foam holder with low dielectric constant ($\epsilon_r = 1.5$). In addition, the tip of the AUT is moved by 4 mm ahead of the edge of the foam as illustrate in Fig. 13(a). A standard gain horn (SGH) antenna is mounted to the scanning arm at the far-field region, which sweeps the surface of a quarter-sphere using two motors programmed through a serial port. Considering the SGH orientation, only co-polarized gain values are measured which correspond to G_θ and G_ϕ for E- and H-plane arcs, respectively.

The CPW side of the antenna feed was excited by network analyser (N5247A PNA-X) via GSG probe. The reference horn

This article has been accepted for publication in a future issue of this journal, but has not been fully edited. Content may change prior to final publication. Citation information: DOI 10.1109/TAP.2014.2364052, IEEE Transactions on Antennas and Propagation

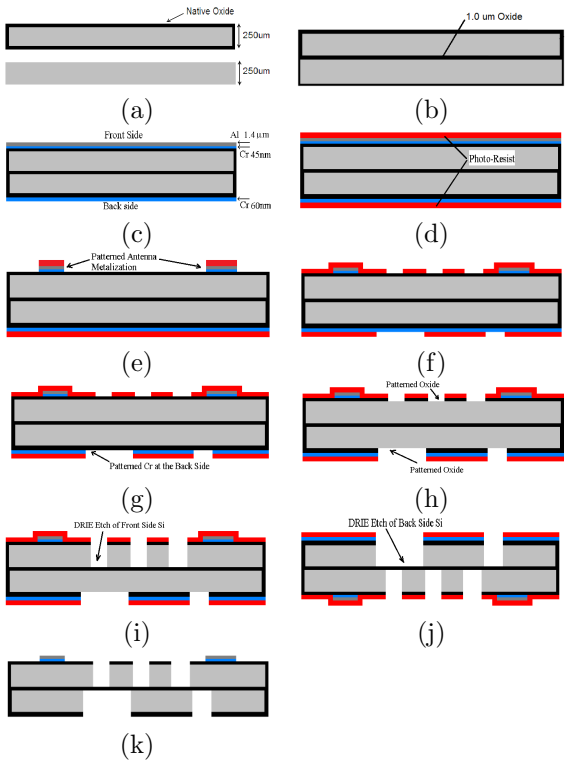

Fig. 11. The fabrication process of the proposed Dielectric Tapered Antenna; (a) first wafer goes into oxidation of 1um then bonded to an un-oxidized wafer, (b) Bonded pair goes to a second run of oxidation to create a permanent bond, (c) Cr/Al and Cr are sputtered on the front and back sides of bonded wafers, respectively, (d) Photo-resist layers are spun coated on both sides, (e) the metallization layer for the antenna is patterned, (f) photo-resist is spun coated on both side and patterned, (g) Cr layer is patterned on the back side, (h) oxide layer is patterned using wet etch, (i) DRIE etch of Si is performed on the front side, (j) DRIE etch is performed on the back side, (k) wafers are cleaned from photo-resists and residue

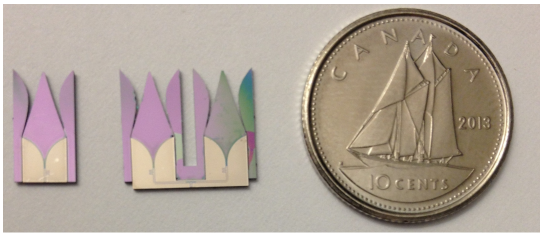

Fig. 12. Fabricated prototypes of single antenna and two-element array antenna.

is connected to the other port of the network analyzer. The setup is calibrated up to A and B nodes with Short-Open-Load-Thru (SOLT) calibration technique, shown in Fig. 13(b). The loss of the probe and cables over the frequency, which are measured separately, are de-embedded from the measured S_{21} results. Although using low-dielectric-constant foam and suspending half of the antenna helps to reduce the pattern deviation, the presence of the foam is also simulated in HFSS to accurately model the measurement situation. Therefore, the simulation results are slightly different from an isolated antenna results presented in Section III.

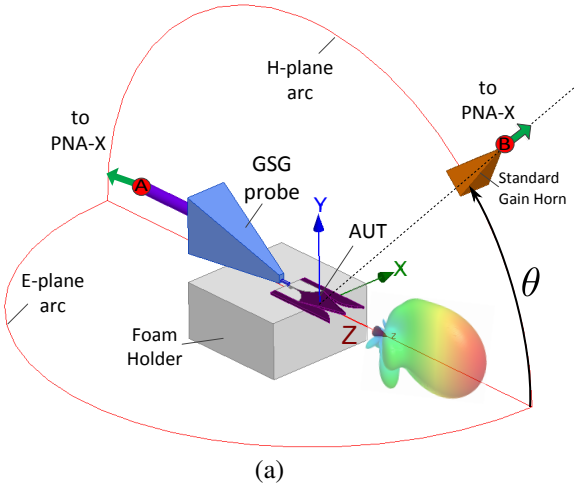

(a)

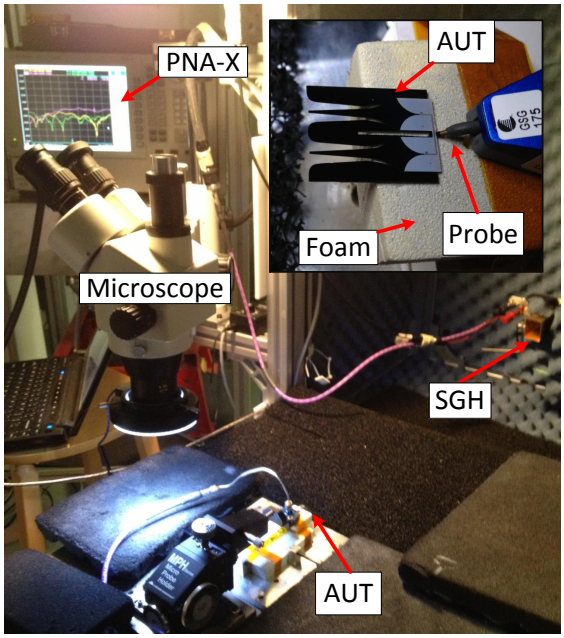

(b)

Fig. 13. (a) Schematic view of measurement setup with the antenna under test (AUT) on a foam holder and a SGH scanning E- and H-plane arcs, (b) photo of the automated measurement setup including a GSG probe, microscope, a SGH connected to a scanning arm inside an anechoic chamber, and a network analyser (PNA-X).

B. Single Antenna Measured Results

The measured and simulated reflection coefficients of the antenna when it is placed on the foam holder are shown in Fig. 14. The results show the 10-dB antenna bandwidth is 14 GHz from 53 GHz to 67 GHz. However, the measured reflection coefficient drops at frequencies beyond 67 GHz which is the operation limit of the PNA-X.

Moreover, Fig. 14 compares the measured and simulated peak gain over the frequency range of 52-67 GHz. The maximum gain of 9.6 dBi is measured at 62 GHz which is 0.5 dB less than the simulated value. This difference is within the measurement error ($\approx$ 1 dB). It is worth mentioning that the simulation of high permittivity materials such as silicon requires very fine meshing to achieve a high accuracy. Furthermore, the measured peak gain, drops faster at lower

This article has been accepted for publication in a future issue of this journal, but has not been fully edited. Content may change prior to final publication. Citation information: DOI 10.1109/TAP.2014.2364052, IEEE Transactions on Antennas and Propagation

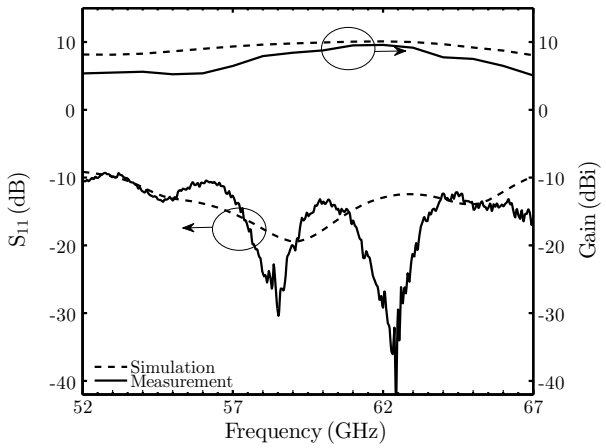

Fig. 14. Simulated and measured results of reflection coefficients and gain for the single antenna.

frequencies comparing with simulation results. The measured co-polarized radiation patterns for single antenna in E- and H-plane arcs are presented in Fig. 15, and well agree with simulations. The reference coordinates for pattern measurements are shown in Fig. 13(a). Since the AUT has an endfire radiation pattern, due to the anechoic chamber limits the measurement is done over the E-plane and H-plane arcs, θ varying from 0 to 180 deg. Therefore, the antenna radiation pattern peaks at $\theta = 0$ deg. Assuming the pattern symmetry with respect to Z-axis on XZ and YZ planes, the measured 3-dB beamwidth of the single element antenna are 40 deg and 70 deg on E- and H-plane, respectively. Since the antenna beam is wider in H-plane, the multipath profile is more significant in this plane compared to E-plane, which causes higher ripples in measured H-plane pattern due to the reflections from uncovered probe and the exposed metal cables seen in Fig. 13(b).

C. Array Antenna Measured Results

The simulated and measured reflection coefficients (S_{11}) of the two-element array antenna are shown in Fig. 16. The measured frequency has shifted 1 GHz to the right, which can be explained by the fabrication tolerances. The measured 10 dB impedance bandwidth is 10 GHz. Moreover, measured and simulated gain vs. frequency results are presented in Fig. 16. Maximum measured gain of 11 dBi occurs at 59 GHz, which is 1 dB less than simulated value.

The measured co-polarized radiation patterns of the two element array on E- and H-plane at 60 GHz are shown in Fig. 17 (a) and (b), respectively. The measured peak gain value for the array antenna is 10.8 dBi which is 1.2 dB less than the simulated value. The beamwidth of the antenna is 20 deg and 60 deg in E- and H-plane, respectively. A null in the E-plane radiation pattern appears at $\theta = 26$ deg because of the array factor with elements spacing equal to 0.6 mm ($\approx 1.2\lambda$).

VI. Conclusion

The design and measurement of a 60 GHz CPW-fed planar dielectric tapered antenna with parasitic elements was presented. The design was optimized to achieve a wide bandwidth

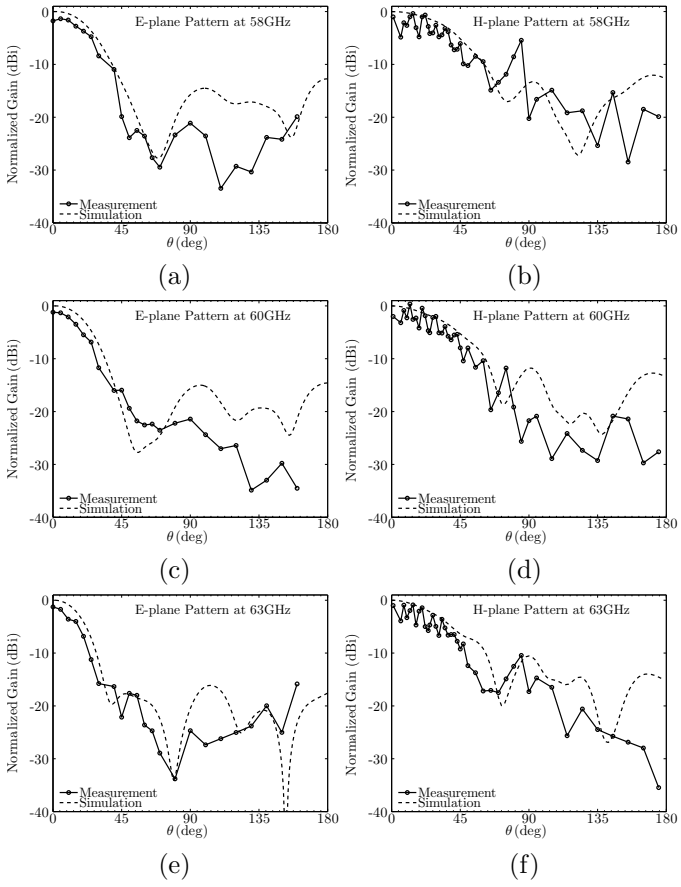

Fig. 15. Simulated and measured co-polarized radiation pattern of single antenna on E-plane and H- plane at (a,b) 58 GHz, (c,d) 60 GHz and (e,f) 63 GHz.

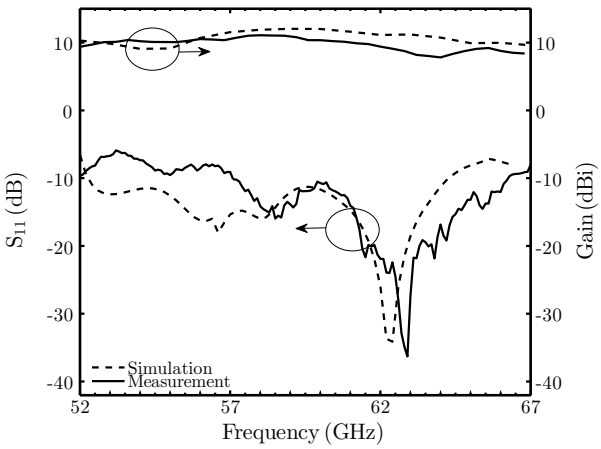

Fig. 16. Simulated and measured results of reflection coefficients and gain for the 2-element array antenna.

more than 14 GHz. Moreover, the two-element array of the proposed antenna was designed using a CPW power divider. A fabrication method compatible with CMOS process was proposed to implement these structures on silicon substrate. The single elements antenna has a compact size of 9.3 mm $\times$ 4.9 mm with a maximum simulated gain of 10.25 dB and a maximum efficiency of 92.5% at 63 GHz. The two-element

This article has been accepted for publication in a future issue of this journal, but has not been fully edited. Content may change prior to final publication. Citation information: DOI 10.1109/TAP.2014.2364052, IEEE Transactions on Antennas and Propagation

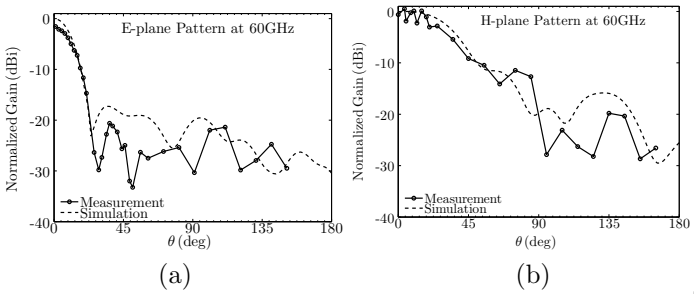

Fig. 17. Simulated and measured co-polarized pattern on (a) E-plane, and (b) H-plane for antenna array.

array demonstrates a maximum simulated gain of 13 dBi and 82% efficiency at 60 GHz with a size of 10.9 mm $\times$ 9.9 mm. The samples were measured using GSG probe station inside an anechoic chamber. Very good agreement between the simulated and experimental results was observed.

ACKNOWLEDGEMENT

This work was supported by National Science and Engineering Research Council (NSERC) of Canada and Research In Motion (RIM).

REFERENCES

[1] L. Verma, M. Fakharzadeh, and S. Choi, "WiFi on steroids: 802.11 ac and 802.11 ad," *Wireless Communications, IEEE*, vol. 20, no. 6, pp. 30–35, 2013.

[2] S. B. Yeap, Z. N. Chen, and X. Qing, "Gain-enhanced 60-GHz LTCC antenna array with open air cavities," *IEEE Trans. Antennas Propag.*, vol. 59, no. 9, pp. 3470–3473, 2011.

[3] X.-P. Chen, K. Wu, L. Han, and F. He, "Low-cost high gain planar antenna array for 60-GHz band applications," *IEEE Trans. Antennas Propag.*, vol. 58, no. 6, pp. 2126–2129, 2010.

[4] A. E. Lamminen, J. Saily, and A. R. Vimpari, "60-GHz patch antennas and arrays on LTCC with embedded-cavity substrates," *IEEE Trans. Antennas Propag.*, vol. 56, no. 9, pp. 2865–2874, 2008.

[5] M. Al Henawy and M. Schneider, "Planar antenna arrays at 60 GHz realized on a new thermoplastic polymer substrate," in *Antennas and Propagation (EuCAP), 2010 Proceedings of the Fourth European Conference on*, 2010, pp. 1–5.

[6] S. Yoshida, Y. Suzuki, T. T. Ta, S. Kameda, N. Suematsu, T. Takagi, and K. Tsubouchi, "A 60-GHz Band Planar Dipole Array Antenna Using 3-D SiP Structure in Small Wireless Terminals for Beamforming Applications," *IEEE Trans. Antennas Propag.*, vol. 61, no. 7, pp. 3502–3510, 2013.

[7] R. A. Alhalabi, Y.-C. Chiou, and G. M. Rebeiz, "Self-Shielded High-Efficiency Yagi-Uda Antennas for 60 GHz Communications," *IEEE Trans. Antennas Propag.*, vol. 59, no. 3, pp. 742–750, 2011.

[8] Z. Sotoodeh, B. Biglarbegian, M. Nezhad-Ahmadi, M. Fakharzadeh, and S. Safavi-Naeini, "A wideband and high gain antenna for short-range mm-wave wireless applications," in *Antennas and Propagation Society International Symposium (APSURSI), 2010 IEEE*, 2010, pp. 1–4.

[9] A. Simba, M. Yamamoto, T. Nojima, and K. Itoh, "Linear array of image NRD guide-based dielectric rod antenna fed by slotted rectangular waveguide," *IEE Proceedings-Microwaves, Antennas and Propagation*, vol. 152, no. 5, pp. 331–336, 2005.

[10] J. Weinzierl, J. Richter, G. Rehm, and H. Brand, "Simulation and measurement of dielectric antennas at 150 GHz," in *Microwave Conference, 1999. 29th European*, vol. 2, 1999, pp. 185–188.

[11] J.-Y. Chung and C.-C. Chen, "Two-layer dielectric rod antenna," *IEEE Trans. Antennas Propag.*, vol. 56, no. 6, pp. 1541–1547, 2008.

[12] G. Adamiuk, T. Zwick, and W. Wiesbeck, "Compact, dual-polarized UWB-antenna, embedded in a dielectric," *IEEE Trans. Antennas Propag.*, vol. 58, no. 2, pp. 279–286, 2010.

[13] A. B. Guntupalli and K. Wu, "Polarization-agile millimeter-wave antenna arrays," in *Microwave Conference Proceedings (APMC), 2012 Asia-Pacific*, 2012, pp. 148–150.

[14] N. Ghassemi and K. Wu, "Planar Dielectric Rod Antenna for Gigabyte Chip-to-Chip Communication," *IEEE Trans. Antennas Propag.*, vol. 60, no. 10, pp. 4924–4928, 2012.

[15] K. Iigusa, K. Li, K. Sato, and H. Harada, "Gain Enhancement of H-Plane Sectoral Post-Wall Horn Antenna by Connecting Tapered Slots for Millimeter-Wave Communication," *IEEE Trans. Antennas Propag.*, vol. 60, no. 12, pp. 5548–5556, 2012.

[16] A. Patrovsky and K. Wu, "Active 60 GHz front-end with integrated dielectric antenna," *Electronics letters*, vol. 45, no. 15, pp. 765–766, 2009.

[17] R. Kazemi, A. E. Fathy, and R. A. Sadeghzadeh, "Dielectric rod antenna array with substrate integrated waveguide planar feed network for wideband applications," *IEEE Trans. Antennas Propag.*, vol. 60, no. 3, pp. 1312–1319, 2012.

[18] F. J. Zucker, "Surface-wave antennas," *Antenna engineering handbook*, pp. 12–1, 2007.

[19] S. Gigoyan, D. Saeedkia, M. Neshat, H. Chen, and S. Safavi-Naeini, "Tapered dielectric image-line antenna array for millimeter-wave applications," in *Radio and Wireless Symposium, 2008 IEEE*, 2008, pp. 667–670.

[20] K.-P. Ma, Y. Qian, and T. Itoh, "Analysis and applications of a new CPW-slotline transition," *IEEE Trans. Microw. Theory Techn.*, vol. 47, no. 4, pp. 426–432, 1999.

[21] A. Rida, A. Margomenos, and M. M. Tentzeris, "Wideband mm-wave compensated 90° bends for Grounded Coplanar Waveguide and microstrip Transmission Lines on flexible LCP substrates," in *Electronic Components and Technology Conference, 2009. ECTC 2009. 59th*, 2009, pp. 2000–2003.

This article has been accepted for publication in a future issue of this journal, but has not been fully edited. Content may change prior to final publication. Citation information: DOI 10.1109/TAP.2014.2364052, IEEE Transactions on Antennas and Propagation

Saman Jafarlou received his B.Sc. from the University of Teharn, Iran, in 2010, and his M.Sc. from the University of Waterloo, Canada, in 2012, both in electrical engineering. He joined Center for Intelligent Antenna and Radio Systems (CIARS) where he worked on nano-photonics and optoelectronic devices for THz applications, besides integrated antennas for 60 GHz application and phased-array systems for satellite communication. He joined Peraso Technologies, Toronto, Canada, a fabless semiconductor company developing 60 GHz wireless chip sets, in 2013. In Peraso, he is working on developing antennas for indoor applications, long-range backhaul modules and exploring different packaging technologies for mm-wave applications.

Maher Bakri-Kassem (S01M06-SM10) was born in Kuwait City, Kuwait, on December 19, 1972. He received his PhD in electrical and computer engineering from the University of Waterloo, Canada in 2007. In 2001, he joined the Center for Integrated RF Engineering (CIRFE), where he was involved with the design, optimization, and fabrication of RF/microwave circuits, RF MEMS devices, and RF MEMS/CMOS integrated circuits. He joined the Research and Development Department, Custom Products Business Unit, MEMSCAP Inc., NC, USA in 2007 where he was involved in developing MEMS devices and circuitry for RF and optical application. In 2009, he joined the University of Waterloo as a post-doctoral fellow. In 2011, he joined the American University of Sharjah where he is currently an Assistant Professor at the Electrical Engineering Department. He authored and co-authored over 20 publications. He has a US patent in the MEMS/CMOS integration and circuits. His research interests are applied electromagnetic, RF, microwave, mm-wave circuits, RF MEMS, RF MEMS/CMOS integration and energy harvesting.

Mohammad Fakharzadeh [SM'12] received his Ph.D. in electrical engineering from the University of Waterloo, Canada, in 2008, and his M.Sc. in electrical engineering from Sharif University of Technology in 2002. He is currently managing the antenna and packaging group at Peraso Technologies, Toronto, Canada, developing millimeter-wave solutions for portable electronic devices and small cell backhaul. He has more than 13 years of experience in design and implementation of phased array antenna systems and millimeter-wave technology, particularly novel antenna and package design. He has authored over 50 scientific papers and 10 patents.

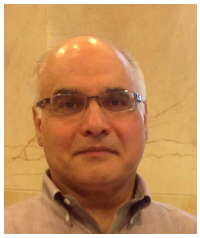

Safieddin (Ali) Safavi-Naeini is a professor with the Department of Electrical and Computer Engineering, University Waterloo, NSERC-BlackBerry Industrial Research Chair in Integrated RF technologies, and the director of the newly established Center for Intelligent Antenna and Radio Systems (CIARS). He has 35+ years of experience and 150+ journal papers and 300+ conference papers in RF/Microwave antenna and circuit technologies, integrated radio and antenna system technologies for a vast range of applications in wireless communications, intelligent miniaturized sensor networks, land-mobile Satcom, radio technologies for Intelligent Transportation Systems (ITS), millimeter-wave/sub-millimeter-wave antenna and integrated circuits, computational electromagnetics, radio-wave propagation analysis and simulation, bio- electromagnetics, and THz technologies. He has led several national and international research collaborations including the ongoing research programs on novel architectures for wireless mmW/THz intelligent radio/antenna for extreme bandwidth communication and sensing, next generation mmW high-resolution radar sensor, and emerging mmW land-mobile satellite communication systems and SOTM.